

Multi-modal Data based Semi-Supervised Learning for Vehicle Positioning

Ouwen Huan , Mingzhe Chen, *Member, IEEE,*
 Yang Yang, *Member, IEEE* , Tao Luo, *Senior Member, IEEE*

Abstract—In this paper, a multi-model data based semi-supervised learning (SSL) framework that jointly use channel state information (CSI) data and RGB images for vehicle positioning is designed. In particular, an outdoor positioning system where the vehicle locations are determined by a base station (BS) is considered. The BS equipped with several cameras can collect a large amount of unlabeled CSI data and a small number of labeled CSI data of vehicles, and the images taken by cameras. Although the collected images contain partial information of vehicles (i.e. azimuth angles of vehicles), the relationship between the unlabeled CSI data and its azimuth angle, and the distances between the BS and the vehicles captured by images are both unknown. Therefore, the images cannot be directly used as the labels of unlabeled CSI data to train a positioning model. To exploit unlabeled CSI data and images, a SSL framework that consists of a pretraining stage and a downstream training stage is proposed. In the pretraining stage, the azimuth angles obtained from the images are considered as the labels of unlabeled CSI data to pretrain the positioning model. In the downstream training stage, a small sized labeled dataset in which the accurate vehicle positions are considered as labels is used to retrain the model. Simulation results show that the proposed method can reduce the positioning error by up to 30% compared to a baseline where the model is not pretrained.

Index Terms—Semi-supervised learning, vehicle positioning, multi-modal data.

I. INTRODUCTION

Vehicle positioning plays an important role for future vehicle applications such as autonomous driving and traffic monitoring [1]. Current global navigation satellite system (GNSS) based vehicle localization methods (e.g. global positioning system (GPS)) have significant performance loss in urban environments due to the blockage of buildings, pedestrians, and vehicles. To improve the accuracy of these vehicle positioning methods, one can study the use of RF for vehicle positioning. Compared to GNSS based positioning methods, RF based sensing methods have lower latency and can achieve higher positioning accuracy in urban areas. However, using RF signals for vehicle positioning still faces several challenges such as high accuracy localization of high-speed moving targets, precise 3-D signal propagation environment modeling

O. Huan and T. Luo are with the Beijing Laboratory of Advanced Information Network, Beijing University of Posts and Telecommunications, Beijing, 100876, China (e-mail: ouwenh@bupt.edu.cn; tluo@bupt.edu.cn).

M. Chen is with the Department of Electrical and Computer Engineering and Institute for Data Science and Computing, University of Miami, Coral Gables, FL, 33146, USA (e-mail: mingzhe.chen@miami.edu).

Y. Yang is with the Beijing Key Laboratory of Network System Architecture and Convergence, School of Information and Communication Engineering, Beijing University of Posts and Telecommunications, Beijing 100876, China (e-mail: yangyang01@bupt.edu.cn).

for localizing non-line-of-sight (NLoS) users, and combination with the traditional GNSS based localization methods.

Recently, a number of existing works [2]–[10] have studied the use of RF data for indoor and outdoor positioning. The work in [2] first presented a hybrid location image fingerprint generated with Wi-Fi and magnetic field fingerprints, and then a convolutional neural network (CNN) was employed to classify the locations of the fingerprint images. The authors in [3] designed a deep learning (DL) based localization algorithm that uses both RSS and channel state information (CSI) for indoor positioning. In [4], a positioning model based on the ResNet architecture [11] is designed to localize users using NLoS transmission links. However, in these works, the RF fingerprints were collected at some fixed locations, and the positioning problem was formulated as a classification problem that classified the locations of user equipments (UE). The works in [5]–[10] formulated positioning as a coordinate regression problem. In [5], a stacked auto-encoder with an one-dimensional CNN was developed to achieve high positioning accuracy using received signal strengths (RSS). The authors in [6] used the angle-delay channel power matrix as the input of a CNN to estimate user positions. In [7], the authors designed an attention-augmented residual CNN with a larger receptive field for user positioning. The authors in [8] designed two effective methods to process CSI for positioning. The work in [9] studied the fingerprint based positioning aided by reconfigurable intelligent surface (RIS). In this work, the authors proposed a new type of fingerprint named space-time channel response vector (STCRV), and designed a novel residual CNN to estimate the 3D positions of targets. In [10], the authors designed a CSI fingerprint based positioning system trained with CSI collected at multiple BSs. However, all of these works [2]–[10] require the use of a large amount of labeled data (i.e. RF data and their corresponding positions) to train DL models, which may not be applied for the scenarios where a server cannot collect such large amount of labeled data.

To improve the performances of DL models and reduce the size of labeled RF dataset for model training, the works in [12]–[18] studied the use of multi-modal data to assist positioning and other RF applications. First, the authors in [12]–[16] investigated the use of multi-modal data including red green blue (RGB) images, light detection and ranging (LiDAR) data, and GPS data in beam selection and blockage prediction. Specifically, the authors in [12] employed an object detection model to localize vehicles and blockages in images, and achieve blockage prediction with a recurrent neural

network (RNN). In [13], the authors leveraged image data to proactively predict dynamic link blockages and handoff for millimeter Wave (mmWave) systems. The authors in [14] and [15] utilized images to achieve fast and low-overhead mmWave/Terahertz (THz) beam tracking. In [16], a fusion-based deep learning framework operating on images, LiDAR data, and GPS data was designed to predict the subset of top-K optimal beam pairs. However, none of these works considered to use multi-modal unlabeled data to generate labeled data for training DL models. Therefore, they still need to collect a large amount of labeled data to train their designed DL models. The works in [17] and [18] studied the joint use of images and wireless data for positioning. In [17], the authors designed an algorithm to fuse the features of wireless data and RGB images to accurately estimate the locations of an indoor smartphone. However, in [17], the RGB images are taken by the smartphone, but not by the cameras equipped at access points (APs) or BSs. Hence, the method in [17] may not be used for a large-scaled outdoor scenario like vehicle positioning, since outdoor scenarios are generally more complex than indoor scenarios, and it is much harder to determine the location of a vehicle with images taken from the vehicle's perspective. The work in [18] introduced an image-driven representation method to represent all the received signals with a specially designed RF image. Then, this RF image was combined with an RGB image captured by the camera for positioning. However, the work in [18] did not consider how to find the correct user position in the RGB image that each RF signal corresponds to since each RGB image may capture the locations of multiple users.

The main contribution of this work is a novel semi-supervised learning (SSL) framework that jointly use images and unlabeled CSI data which can be collected at a lower cost to improve the performance of the vehicle positioning model in an outdoor environment. The key contributions include:

- We propose a novel SSL framework that jointly uses images, unlabeled data and labeled data to estimate the locations of multiple vehicles. The proposed SSL framework consists of a pretraining stage and a downstream training stage. In the pretraining stage, we consider the information of vehicle positions obtained from the image data as the labels of CSI data to pretrain a part of the positioning model. Then, in the downstream training stage, a small-sized labeled dataset in which the precise vehicle positions are considered as labels is used to retrain the model.
- We consider the problem of the unknown corresponding relationship between unlabeled CSI data and vehicles detected from images. Specifically, in the considered vehicle positioning scenario, the vehicle locations are determined by a BS equipped with a set of cameras. The BS can collect a large amount of unlabeled CSI data, the images taken by cameras, and a small number of labeled CSI data due to the cost of data collection. Although the collected images contain partial information of multiple vehicle positions (i.e. azimuth angles of vehicles), we know neither the corresponding relationship between the

TABLE I: List of notations

Notation	Description
V_t	Number of vehicles served as time t
$x_{t,m}^k$	Symbol transmitted to vehicle m over subcarrier k at time t
$y_{t,m}^k$	Received symbol from vehicle m over subcarrier k at time t
$\mathbf{f}_{t,m}$	Beamforming vector of $x_{t,m}^k$
$\mathbf{h}_{t,m}$	Channel from BS to vehicle m over subcarrier k at time t
$n_{t,m}^k$	Additive Gaussian noise
σ_k^n	Variance of noise
N_B	Antenna number of ULA
N_C	Number of OFDM sub-carriers
$\mathbf{H}_{t,m}$	CSI matrix of vehicle m at time t
\mathbf{H}_t	CSI matrices collected by the BS at time t
C	Number of cameras equipped at BS
$\mathbf{I}_{t,c}$	RGB image captured by camera c at time t
\mathcal{I}_t	Set of RGB images captured at time t
W_c	Width of images captured by camera c
H_c	Height of images captured by camera c
(o^w, x^w, y^w, z^w)	World coordinate system
(o^i, x^i, y^i)	Image coordinate system
(o^p, u^p, v^p)	Pixel coordinate system
$[u_m^p, v_m^p]^T$	Pixel coordinate of point m
ϕ	Azimuth angle of point m
θ	Elevation angle of point m
ϕ_c^L	Azimuth angle of the LoS direction of camera c
θ_c^L	Elevation angle of the LoS direction of camera c
$\Delta\phi$	Difference between ϕ and ϕ_c^L
$\Delta\theta$	Difference between θ and θ_c^L
V'_t	Number of vehicles detected from images in \mathcal{I}_t
$\phi_{t,i}$	Azimuth angle of vehicle i detected from images
q_t	Vector contains the azimuth angles of vehicles captured by the images in \mathcal{I}_t

unlabeled CSI data and azimuth angles, nor the distances between the BS and the vehicles captured by images. In consequence, the information of vehicle positions obtained from images cannot be directly used as the labels of unlabeled CSI data to train a positioning model.

- To solve this problem, we propose a weakly-supervised learning scheme to pretrain our DL model. In particular, we first transform each set of image into a probability distribution vectors of vehicles in angular domain according to the noisy-or (NOR) [19] model. Then, we formulate the pretraining goal as predicting the probability distribution vectors of vehicles.

Simulation results show that the proposed method can significantly reduce the positioning error by up to 30% especially when the amount of labeled data is small compared to a baseline where the model is not pretrained. To our best knowledge, this is the first work that considers joint use of CSI data and camera images for vehicle positioning.

The rest of this paper is organized as follows. The system model of the considered outdoor vehicle positioning system which includes the radio frequency CSI collection and images

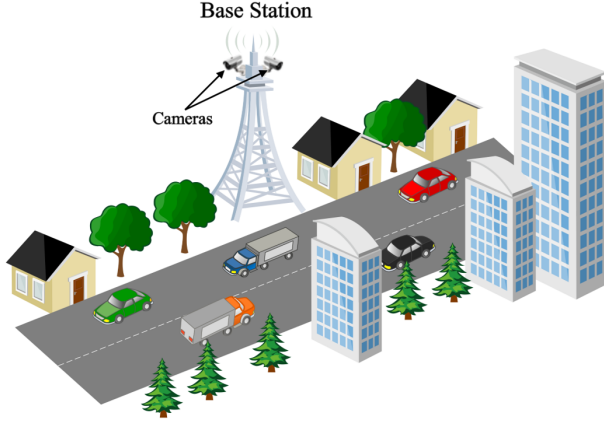


Fig. 1: Considered outdoor positioning scenario.

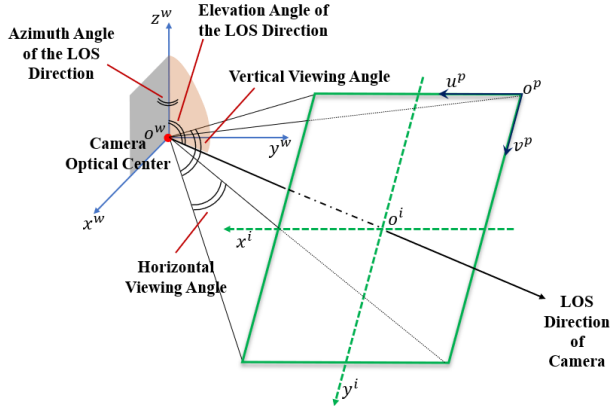


Fig. 2: Diagram of camera FoV.

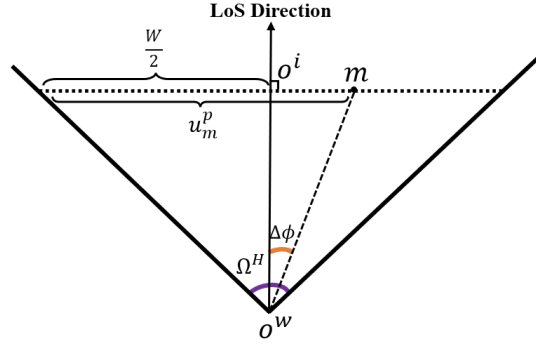
acquisition and processing are described in Section II. Section III introduces the proposed SSL framework which can jointly use images and unlabeled CSI data to improve the performance of the positioning model. In Section IV, numerical results are presented and discussed. Finally, conclusions are drawn in Section V.

II. SYSTEM MODEL

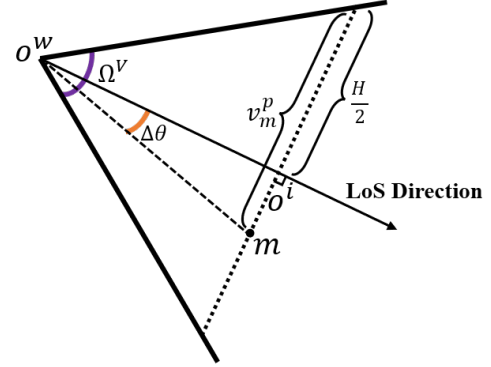
As shown in Fig. 1, we consider an outdoor millimeter wave (mmWave) positioning system where the locations of vehicles are determined with one single BS. In particular, the BS is equipped with a set of C cameras and can use both images captured by its cameras and CSI received from vehicles for vehicle positioning. To localize vehicles, the BS will first send a pilot signal to the vehicles which will send their estimated CSI information back to BS. Then, the BS can use both CSI information and images captured by their cameras to determine the locations of vehicles. Next, we will first introduce radio frequency CSI collection. Then, we introduce the images acquisition and processing in detail.

A. Radio Frequency CSI Collection

We assume that the BS is serving V_t vehicles at time t . The symbol transmitted by the BS to vehicle m over subcarrier k



(a) Horizontal section of camera FoV



(b) Vertical section of camera FoV

Fig. 3: Horizontal and Vertical Sections of FoV

at time t is $x_{t,m}^k \in \mathbb{C}^{1 \times 1}$. Then, the received symbol $y_{t,m}^k$ of vehicle m is

$$y_{t,m}^k = (\mathbf{h}_{t,m}^k)^T \mathbf{f}_{t,m} \cdot x_{t,m}^k + n_{t,m}^k, \quad (1)$$

where $\mathbf{h}_{t,m}^k \in \mathbb{C}^{N_B \times 1}$ is the channel from BS to the vehicle m with N_B being the number of antennas of the uniform linear array (ULA) at BS [20]. $\mathbf{f}_{t,m}$ is the beamforming vector [21]. $n_{t,m}^k$ is an additive received noise following a zero-mean Gaussian distribution with a variance σ_k^n . Without loss of generality, we suppose that the variance of noise is time-invariant. When $x_{t,m}^k$ belongs to a predefined pilot signal known by both BS and vehicle, the channel $\mathbf{h}_{t,m}^k$ can be estimated at the vehicle based on the received symbol $y_{t,m}^k$ and will be transmitted back to BS. The received CSI matrix at BS is expressed as

$$\mathbf{H}_{t,m} = [\mathbf{h}_{t,m}^1, \mathbf{h}_{t,m}^2, \dots, \mathbf{h}_{t,m}^{N_C}] \in \mathbb{C}^{N_B \times N_C}, \quad (2)$$

where N_C is the number of valid subcarriers. We store the CSI matrices collected by the BS at current time t into a three-dimensional matrix as $\mathbf{H}_t = [\mathbf{H}_{t,1}, \mathbf{H}_{t,2}, \dots, \mathbf{H}_{t,V_t}] \in \mathbb{C}^{V_t \times N_B \times N_C}$. We assume that most of the served vehicles cannot provide their position information to the BS when uploading their CSI, which indicates that the collected CSI will constitute a large unlabeled dataset and a small labeled dataset for training a CSI fingerprint based positioning model.

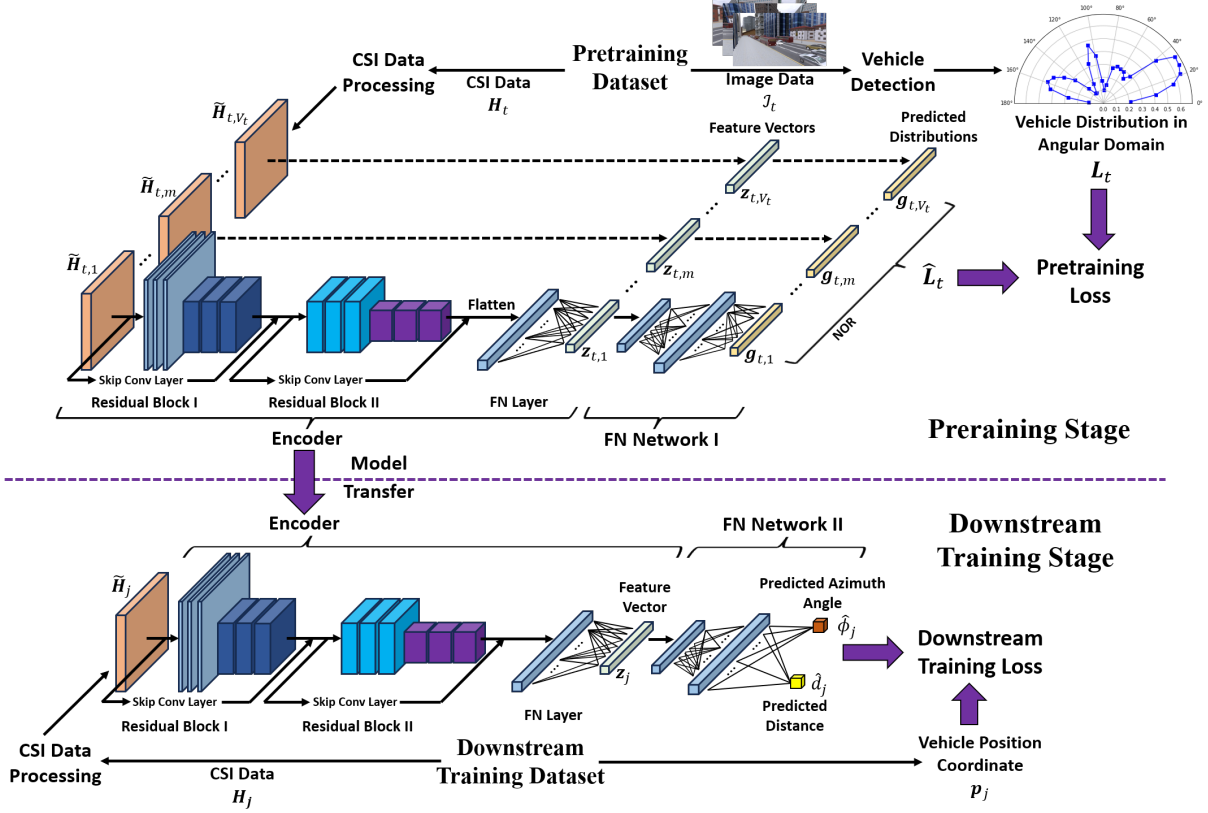


Fig. 4: Architecture of the proposed SSL framework.

B. Image Acquisition and Processing

The BS is equipped with a set of C cameras which will capture C images at each time slot to achieve wider field of view (FoV) coverage. The set of images captured at time t is

$$\mathcal{I}_t = \{\mathbf{I}_{t,c} | c = 1, 2, \dots, C\}, \quad (3)$$

where $\mathbf{I}_{t,c}$ is the RGB image captured by camera c at time t . We assume that all images taken by camera c have the same dimension of $3 \times W_c \times H_c$ with W_c and H_c respectively being the width and height of images.

To explain the use of images for vehicle positioning, we first introduce three coordinate systems shown in Fig. 2, which are the 3D world coordinate system (WCS) (o^w, x^w, y^w, z^w) , the 2D image coordinate system (ICS) (o^i, x^i, y^i) and the 2D pixel coordinate system (PCS) (o^p, u^p, v^p) [22], [23]. Both the ICS and PCS are on the image plane but have their own coordinate origins (i.e. $o^i \neq o^p$). In particular, we assume that both axis $o^p u^p$ and axis $o^i x^i$ are parallel to plane $x^w o^w y^w$. Given the line-of-sight (LoS) direction and viewing angles of a camera, each pixel on the image plane can be transformed to a polar coordinate $[\phi, \theta]$ in the WCS where ϕ and θ respectively denote the azimuth and elevation angles [24]. The coordinate transformation from pixel coordinate in PCS to polar coordinate in WCS is summarized in the following lemma.

Lemma 1: Given the pixel coordinate of point m as $[u_m^p, v_m^p]^T$, the azimuth angle ϕ and elevation angle θ of point

m in WCS are

$$\begin{bmatrix} \phi \\ \theta \end{bmatrix} = \begin{bmatrix} \phi^L \\ \theta^L \end{bmatrix} + \begin{bmatrix} \arctan\left(\frac{2u_m^p - W}{W} \tan \frac{\Omega^H}{2}\right) \\ \arctan\left(\frac{2v_m^p - H}{H} \tan \frac{\Omega^V}{2}\right) \end{bmatrix}, \quad (4)$$

where ϕ^L and θ^L respectively denote the azimuth and elevation angles of the LoS direction of the camera. Ω^H and Ω^V respectively represent the camera's horizontal and vertical viewing angles. W and H are the width and height of the pixel plane.

Proof: To determine the azimuth and elevation angles of point m , we first need to calculate the azimuth angle difference $\Delta\phi = \phi - \phi^L$ and the elevation angle difference $\Delta\theta = \theta - \theta^L$ between the direction of point m and the camera LoS direction $[\phi^L, \theta^L]$. According to the horizontal section and vertical section of the camera FoV as shown in Fig. 3, we have

$$\frac{\tan \Delta\phi}{\tan \frac{\Omega^H}{2}} = \frac{u_m^p - \frac{W}{2}}{\frac{W}{2}}, \quad (5)$$

and

$$\frac{\tan \Delta\theta}{\tan \frac{\Omega^V}{2}} = \frac{v_m^p - \frac{H}{2}}{\frac{H}{2}}. \quad (6)$$

Given (5) and (6), we have

$$\begin{bmatrix} \tan \Delta\phi \\ \tan \Delta\theta \end{bmatrix} = \begin{bmatrix} \frac{u_m^p - \frac{W}{2}}{\frac{W}{2}} \tan \frac{\Omega^H}{2} \\ \frac{v_m^p - \frac{H}{2}}{\frac{H}{2}} \tan \frac{\Omega^V}{2} \end{bmatrix}. \quad (7)$$

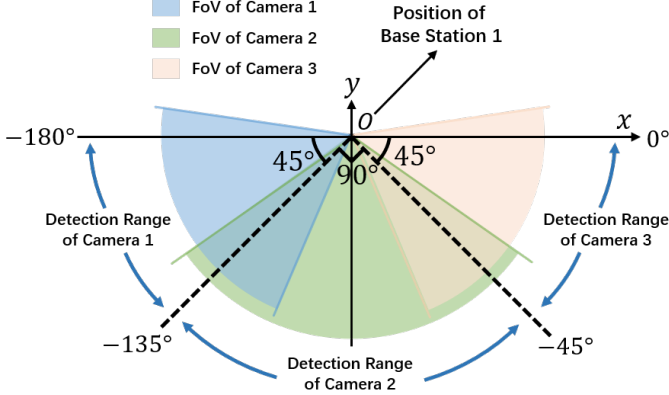


Fig. 6: Detection ranges of different cameras.

We then combine all $\tilde{\mathbf{H}}_{t,m}$ into a four-dimensional matrix $\tilde{\mathbf{H}}_t$ given by

$$\tilde{\mathbf{H}}_t = [\tilde{\mathbf{H}}_{t,1}, \tilde{\mathbf{H}}_{t,2}, \dots, \tilde{\mathbf{H}}_{t,V_t}] \in \mathbb{R}^{V_t \times 3 \times N_B \times N_C}. \quad (14)$$

where V_t denotes the number of original CSI matrices in \mathbf{H}_t .

For the downstream training dataset \mathcal{D}_T and validation dataset \mathcal{D}_d , we respectively transform the complex-valued CSI matrices $\mathbf{H}_j, \mathbf{H}_j^d$ to real-valued three-dimensional matrices $\tilde{\mathbf{H}}_j, \tilde{\mathbf{H}}_j^d \in \mathbb{R}^{3 \times N_B \times N_C}$ using the same method for processing $\mathbf{H}_{t,m}$ as described in (11) and (12).

2) *Vehicle Azimuth Angle Vector Processing*: Next, we explain the use of the images collected by the BS at each time slot to generate the labels for our pretraining. We first use the YOLOv4 model to detect vehicles from images in \mathcal{I}_t and transform their pixel coordinates into polar coordinates according to Lemma 1. We assume that the detection ranges of different cameras are not overlapped as shown in Fig. 6 such that a vehicle will not be captured by several cameras. Despite each \mathbf{H}_t consists of the CSI matrices of V_t vehicles and \mathbf{q}_t contains the azimuth angles of V'_t vehicles, we do not know their corresponding relationship, which can be termed as a multi-instance multi-label learning problem according to [27] and [28]. To solve this problem, we make \mathbf{q}_t into a probability distribution vector given by

$$\mathbf{L}_t = [l_{t,1}, \dots, l_{t,k}, \dots, l_{t,K}] \in \mathbb{R}^{1 \times K}, \quad (15)$$

where $l_{t,k}$ represents the probability of a vehicle at direction k . Specifically, we assume that the direction-finding (DF) range of our ULA is from 0° to Ω° , and it is divided into K intervals with a same size of $\omega = \frac{\Omega}{K}$. Then, the probability of the azimuth angle $\phi_{t,i}$ at each direction is represented by a Gaussian distribution with $\phi_{t,i}$ and ω respectively being the mean value and standard deviation, which can be expressed as

$$\mathbf{w}_{t,i} = \left[w_{t,i,1}, \dots, w_{t,i,k}, \dots, w_{t,i,K} \right] = \frac{1}{\sum_{k=1}^K e^{-\frac{(c_k - \phi_{t,i})^2}{2\omega^2}}} \left[e^{-\frac{(c_1 - \phi_{t,i})^2}{2\omega^2}}, \dots, e^{-\frac{(c_K - \phi_{t,i})^2}{2\omega^2}} \right] \in \mathbb{R}^{1 \times K}, \quad (16)$$

where $w_{t,i,k}$ is the probability of $\phi_{t,i}$ in direction k , and $c_k = (k - \frac{1}{2})\omega$ denotes the center of interval k . Since the

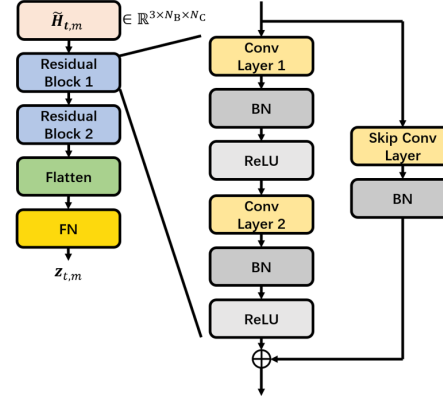


Fig. 7: Structure of the encoder.

distributions of different vehicles are independent, we use the element-wise noisy-or (NOR) model [19] to represent \mathbf{L}_t , which is given by

$$\mathbf{L}_t = \mathbf{1} - (\mathbf{1} - \mathbf{w}_{t,1}) \odot \dots \odot (\mathbf{1} - \mathbf{w}_{t,V'_t}), \quad (17)$$

where $\mathbf{1} = \{1\}^{1 \times K}$ is the $\mathbf{1}$ -vector and \odot denotes the element-wise product.

B. Components of The Proposed Positioning Scheme

Next, we introduce the components of our designed positioning scheme which consists of three components: 1) encoder, 2) FN network I, 3) FN network II. Those components are specified as follows:

1) *Encoder*: The encoder network with parameter ξ_E is used to transform each $\tilde{\mathbf{H}}_{t,m}$ or $\tilde{\mathbf{H}}_j$ into a low-dimensional feature vector [29], [30]. Specifically, we respectively use $\mathbf{z}_{t,m} \in \mathbb{R}^{1 \times N}$ or $\mathbf{z}_j \in \mathbb{R}^{1 \times N}$ to represent the feature vector of each $\tilde{\mathbf{H}}_{t,m}$ or $\tilde{\mathbf{H}}_j$ with N being the output dimension of the encoder. As shown in Fig. 7, the encoder consists of two residual blocks (RBs) and a fully connected (FN) layer [31]. Each RB consists of two convolutional layers and a skip shortcut. The output of the second RB are flattened and fed into an FN layer which will calculate the corresponding feature vector of the input CSI matrix.

2) *FN Network I*: The FN network I with parameter ξ_{F_1} is only used in the pretraining stage. As shown in Fig. 8, the input of FN network I is a feature vector $\mathbf{z}_{t,m}$ encoded from CSI matrix $\mathbf{H}_{t,m}$ in the pretraining dataset. The output of FN network I is a predicted probability distribution in the angular domain given by

$$\mathbf{g}_{t,m} = [g_{t,m,1}, \dots, g_{t,m,k}, \dots, g_{t,i,K}] \in \mathbb{R}^{1 \times K}, \quad (18)$$

where $g_{t,m,k}$ represents the predicted probability of the vehicle corresponding to $\mathbf{H}_{t,m}$ at direction k .

3) *FN Network II*: The FN network II with parameter ξ_{F_2} is only used in the downstream training stage to predict the polar coordinate $\hat{\mathbf{p}}_j = [\hat{\phi}_j, \hat{d}_j] \in \mathbb{R}^{1 \times 2}$ of each $\tilde{\mathbf{H}}_j$ from downstream training dataset according to its feature vector \mathbf{z}_j , where $\hat{\phi}_j \in [0, \Omega]$ is the predicted azimuth angle and $\hat{d}_j \geq 0$ is the predicted horizontal distance between a vehicle and the

scheme with a batch size B_T .

D. Complexity of the Proposed SSL Framework

In this section, we analyze the complexity of the proposed SSL framework. The complexity of the proposed framework is analyzed from three parts: 1) the complexity of pretraining, 2) the complexity of downstream training stage, and 3) the complexity of inference. Specifically, the pretraining process and downstream training process will be respectively conducted once in each iteration during the offline phase, while the inference process of predicting vehicle positions is conducted for each vehicle during the online phase. Next, we first introduce the complexity of pretraining. Then, we explain the complexity of downstream training. Finally, we introduce the complexity of inference.

1) *Complexity of Pretraining:* The complexity of pretraining lies in computing the feature vector $\mathbf{z}_{t,m}$ using the encoder and calculating the distribution vector $\hat{\mathbf{L}}_t$ using FN network I. Since the encoder network consists of two RBs and a FN layer, the complexity of feature vector computation depends on the input and output channels of the convolutional layers in each RB, the spatial sizes of the convolutional kernels, the output widths and lengths of each convolutional layer, and the output dimension of the FN layer. According to [33], the complexity of feature vector computation is given by

$$\begin{aligned} \mathcal{O}\left(B_P\bar{V}\left(\sum_{i=1}^2\left(\sum_{j=1}^2\left((c_{i,j-1}s_{i,j}^2+2)c_{i,j}\alpha_{i,j}\beta_{i,j}\right)\right.\right. \\ \left.\left.+ (c_{i,0}s_i^{*2}+2)c_{i,2}\alpha_{i,2}\beta_{i,2}\right)+\alpha_{2,2}\beta_{2,2}N\right)\right) \quad (27) \\ = \mathcal{O}\left(\max_{i,j}\left((c_{i,j-1}s_{i,j}^2+2)c_{i,j}\right)\right), \end{aligned}$$

where $c_{i,j}$ and $s_{i,j}$ respectively denote the output channel and kernel size of convolutional layer j in RB i , $c_{i,0}$ is the input channel of the first convolutional layer in RB i , $\alpha_{i,j}, \beta_{i,j}$ are the output width and length of convolutional layer j in RB i , s_i^* is the skip convolutional layer kernel size of RB i , and $\bar{V} = \frac{1}{N_p}\sum_{t=t_1}^{t_{N_p}}V_t$ denote the average number of CSI matrices in each \mathbf{H}_t . Given the feature vectors, the complexity of calculating the vehicle distribution vectors in each horizontal direction using FN network I is $\mathcal{O}(B_P\bar{V}(NM_{F_1}+KM_{F_1})) = \mathcal{O}(M_{F_1}(N+K))$, where M_{F_1} represents the number of neurons in the first FN layer of FN network I. Therefore, the computational complexity of the pretraining stage is given by

$$\mathcal{O}\left(\max_{i,j}\left((c_{i,j-1}s_{i,j}^2+2)c_{i,j}\right)+M_{F_1}(N+K)\right). \quad (28)$$

2) *Complexity of Downstream Training:* The complexity of the downstream training stage lies in computing the feature vector \mathbf{z}_j using encoder and determining the polar coordinate $\hat{\mathbf{p}}_j$ with FN network II. Therefore, the computational complex-

TABLE II: System Parameters & Simulation Settings

Parameter	value	Parameter	Value
C	3	Ω	180°
W_c ($c = 1, 2, 3$)	1280	N	32
H_c ($c = 1, 2, 3$)	720	K	15,30,60
N_B	16	B_P	64
N_C	52	B_T	32
N_p	3000	$\lambda_E, \lambda_{F1}, \lambda_{F2}$	10^{-3}
N_V	1480	λ'_E	$\frac{1}{20} \times 10^{-3}$
N_T	200,300,500, 750,1000		

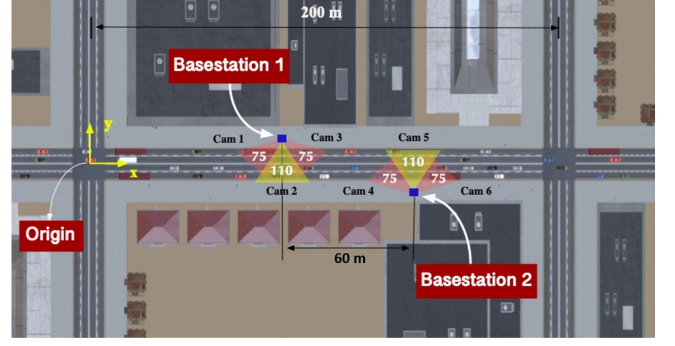


Fig. 9: Scenario of the dataset [33].

ity is

$$\mathcal{O}\left(\max_{i,j}\left((c_{i,j-1}s_{i,j}^2+2)c_{i,j}\right)+M_{F_2}(N+K)\right), \quad (29)$$

where M_{F_2} represents the number of neurons in the first FN layer of FN network II.

3) *Complexity for Inference:* The complexity of inference lies in predicting the vehicle polar coordinates using encoder and FN network II. Compared with downstream training, we do not need to calculate the variance and mean value of each batch of data. Hence, the inference complexity of predicting the position of a vehicle is

$$\mathcal{O}\left(\max_{i,j}\left((c_{i,j-1}s_{i,j}^2+1)c_{i,j}\right)+M_{F_2}(N+K)\right). \quad (30)$$

IV. SIMULATION RESULTS AND ANALYSIS

Next, we evaluate the performance of our proposed scheme on a public dataset called vision-sireless (ViWi) dataset [34]. We first introduce the ViWi dataset. Then, we describe the baselines used in our experiments. Finally, we analyze the performance of our proposed scheme.

A. Dataset

As shown in Fig. 9, the datasets used in simulations are collected from a downtown scenario with multiple served vehicles and two BSs located at each side of the street. All vehicles are located within a 180-degree range in front of each BS. Each BS is equipped with three differently-oriented cameras such that their FoVs can cover the whole street. We only use the dataset collected from the vehicles that are captured by BS 1. The distances between BS 1 and these

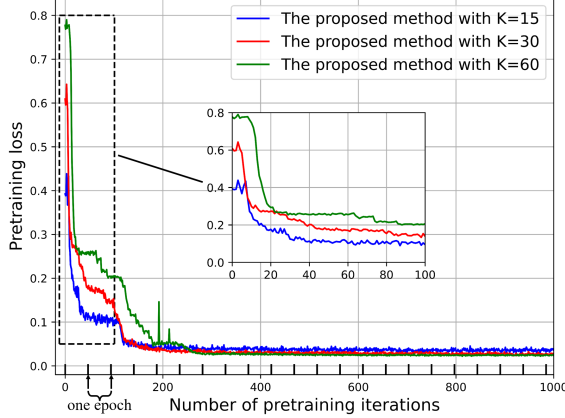


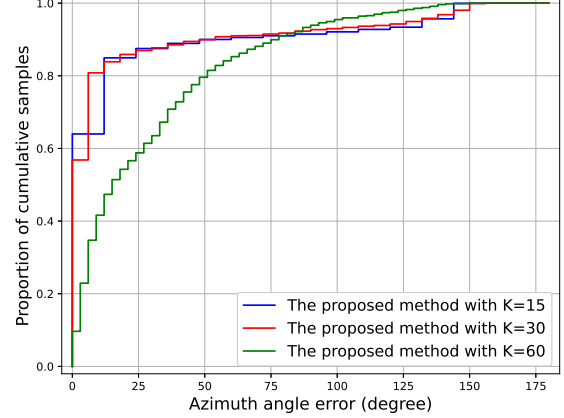
Fig. 10: The convergence of proposed algorithm with different K .

vehicles are no more than 40 m. Each sample consists of three images taken by three cameras, and the CSI matrices and position coordinates of the served vehicles. Since the time slots of two successive samples are very close, we only take one sample from every four samples. After down-sampling and filtering out the unusable samples, we finally select 4000 samples from the dataset. 3000 samples are randomly selected as the pretraining dataset \mathcal{D}_P . The remaining 1000 samples are used as the labeled CSI dataset \mathcal{D}_T and validation dataset. During pretraining, the number of iteration is 3000 and the initial learning rates will be reduced to their 90% by every 100 iterations. In downstream training stage, the model is retrained by 3000 epochs and the learning rates will be reduced to 90% by every 100 epochs. Here, one epoch includes $\frac{N_P}{B_P}$ iterations since an epoch represents the process that the model is once trained by the whole dataset, while an iteration is the process that the model parameters are updated by a mini-batch of data samples. Other system parameters and simulation settings are listed in Table II. For comparison purposes, we consider two baselines. In baseline a), the encoder is randomly initialized and trained only by the labeled dataset \mathcal{D}_T without using the unlabeled dataset \mathcal{D}_P . In baseline b), the encoder is pretrained with the self-supervised contrastive learning (SSCL) scheme [26] using \mathcal{D}_P . Here, the data augmentation of SSCL is achieved by adding Gaussian noise to the original CSI data. Since the encoder of the baseline is not pretrained in baseline a), both the initial learning rates of the encoder and FN network II are 10^{-3} . The number of epochs to train the baseline model is 3000 and the learning rate will be reduced to its 90% by every 100 epochs.

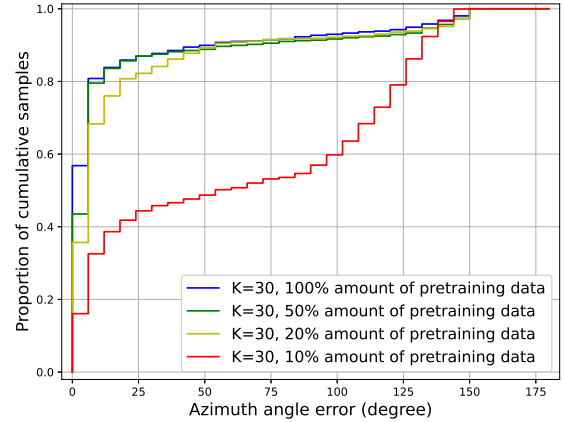
B. Evaluation Metrics

In our experiment, we measure the performances of pretraining and downstream training by calculating their evaluation metrics on a validation dataset $\mathcal{D}_V = \{\mathbf{H}_j, \mathbf{p}_j\}_{j=1}^{N_V}$ that includes N_V labeled samples.

In pretraining stage, we use the azimuth angle error between predicted and ground truth directions to measure the



(a) CDF of azimuth angle error with different K .



(b) CDF of azimuth angle error with different amount of pretraining data ($K = 30$).

Fig. 11: CDF of predicted and ground truth azimuth angle error with different pretraining settings.

performance of our model. Given CSI sample j from \mathcal{D}_V , the azimuth angle error is defined as

$$s_j = \omega \cdot |r_j - \hat{r}_j|, \quad (31)$$

where $r_j = \lceil \frac{\phi_j}{\omega} \rceil$ is the ground truth direction and $\lceil \cdot \rceil$ denotes the round up operation, $\hat{r}_j = \arg \max_{k=1, \dots, K} g_{j,k}$ represents the predicted direction of the vehicle.

In the downstream training stage, we first use mean absolute error (MAE) [35] to measure the performances of vehicle azimuth angle predictions and the predictions of distances between vehicles and the BS of the considered methods, as follows:

$$S_{\text{MAE}}^A = \frac{1}{N_V} \sum_{j=1}^{N_V} |\phi_j - \hat{\phi}_j|, \quad (32)$$

$$S_{\text{MAE}}^D = \frac{1}{N_V} \sum_{j=1}^{N_V} |d_j - \hat{d}_j|. \quad (33)$$

Then, to evaluate positioning accuracy, we use the mean

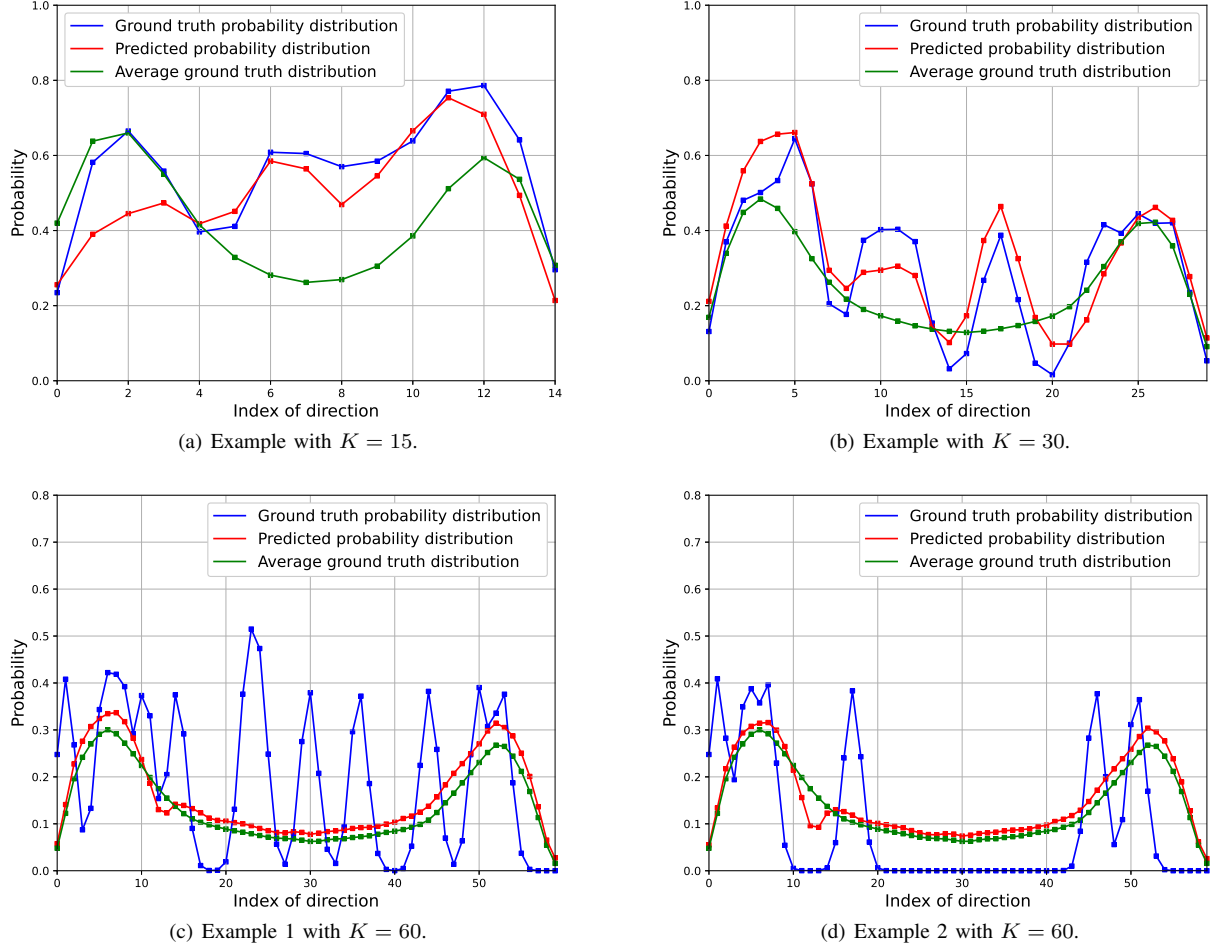


Fig. 12: Examples of ground truth and predicted probability distributions with different K .

Euclidean distance between the predicted and ground truth positions as the positioning error to evaluate the positioning accuracy [36], which is given by $S_{\text{pos}} = \frac{1}{N_V} \sum_{j=1}^{N_V} \|\mathbf{p}_j - \hat{\mathbf{p}}_j'\|_2$.

C. Performance Evaluation

1) *Pretraining*: In Fig. 10, we show how the pretraining loss changes as the number of training iterations increases. From Fig. 10, we see that the pretraining loss of all considered methods remain unchanged when the number of iterations is larger than 250 which implies that all considered algorithms converge after 250 iterations. We can also observe that the pretraining loss of the proposed algorithm with $K = 60$ has the largest initial loss and the lowest descending rate, while the proposed algorithm with $K = 15$ has the smallest initial loss and the highest descending rate. This is because as K increases, the number of components in the predicted probability distribution vector increases, which may increase the difficulties of finding the optimal model that can accurately predict the directions of vehicles.

Fig. 11 shows cumulative distribution function (CDF) of the azimuth angle errors in validation dataset resulting from the proposed algorithms with different configurations. In Fig. 11 (a), we show CDF of the proposed algorithms with $K =$

15, 30, 60 and are trained by the whole pretraining dataset. From Fig. 11 (a), we see that 47% of azimuth angle errors resulting from the algorithm with $K = 60$ are below 12° , and 85% of azimuth angle errors of the algorithm with $K = 15$ or 30 are lower than 12° . This is because when $K = 60$, the proposed algorithm might fail to find the globally optimal model, but converge to a locally optimal solution. From Fig. 11 (a), we also see that 82% of azimuth angle errors of the algorithm with $K = 30$ are below 6° , but only 64% of azimuth angle errors of the algorithm with $K = 15$ are lower than 6° . This is because as K grows from 15 to 30, the size of an azimuth angle interval $\omega = \frac{\Omega}{K}$ in the probability distribution vector will decrease from 12° to 6° . Hence, the accuracy of azimuth angle prediction resulting from the proposed method increases. In Fig. 11 (b), we show the CDF of the proposed algorithms ($K = 30$) that are trained by 100%, 50%, 20%, and 10% amount of pretraining data. From Fig. 11 (b), we observe that 31% of azimuth angle errors of the algorithm that is trained by 10% of pretraining data are lower than 12° . Meanwhile, 85% of azimuth angle errors of the algorithm that is trained by the whole pretraining dataset are below 12° . This is because the model is overfitting on the pretraining dataset when the amount of pretraining data is small [37]. Therefore,

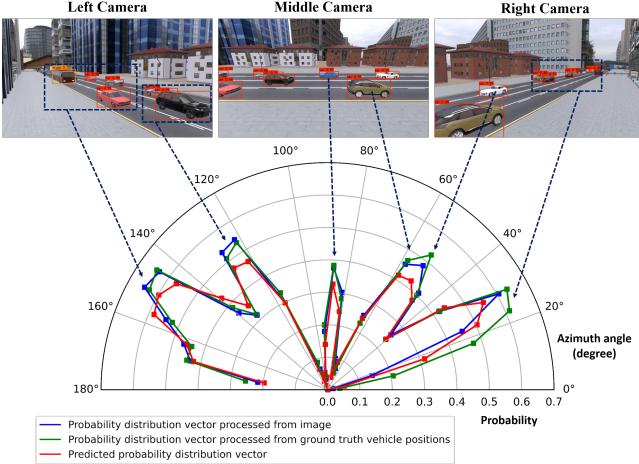


Fig. 13: Probability distribution vectors and detected vehicles in corresponding images.

the accuracy of azimuth angle prediction resulting from the proposed method decreases.

In Fig. 12, we verify the statement that the pretraining algorithm with $K = 60$ might converge to a locally optimal solution rather than the globally optimal model. In this figure, we show the ground truth distribution vector \mathbf{L}_t , the predicted distribution vector $\hat{\mathbf{L}}_t$, and the average ground truth distribution vector $\bar{\mathbf{L}} = \frac{1}{N_p} \sum_{t=1}^{t=N_p} \mathbf{L}_t$. If the algorithm converges to a globally optimal solution, the predicted distribution vector $\hat{\mathbf{L}}_t$ should be close to its ground truth distribution vector \mathbf{L}_t since the target of the pretraining algorithms is to minimize the error between each $\hat{\mathbf{L}}_t$ and \mathbf{L}_t in \mathcal{D}_P . Figs. 12 (a) and (b) show that the $\hat{\mathbf{L}}_t$ is very close to \mathbf{L}_t when the model is pretrained by the algorithm with $K = 15$ or 30 . This is because the algorithm with $K = 15$ or 30 converges to a globally optimal model that can accurately predict the direction of each vehicle. In contrast, in Figs. 12 (c) and (d), $\hat{\mathbf{L}}_t$ are both very close to the average ground truth distribution vector $\bar{\mathbf{L}}$ rather than \mathbf{L}_t . This is because when $K = 60$, the difficulty of finding the globally optimal solution increases. Therefore, the algorithm with $K = 60$ converges to a locally optimal model which maps all the different input data to the same average ground truth distribution vector $\bar{\mathbf{L}}$.

In Fig. 13, we show an example of azimuth angle prediction in validation dataset. Specifically, we show the vehicle detection results of the images, the probability distribution vector obtained from images, the probability distribution vector calculated via ground truth positions of vehicles, and the predicted distribution vector. From Fig. 13, we can see that the probability distribution vector obtained from images is very close to the probability distribution vector resulting from the ground truth positions of vehicles, which verifies the feasibility of using image data to generate labels for unlabeled CSI data. We can also observe from Fig. 13 that the predicted probability distribution vector is similar to the other two vectors. This implies that the proposed pretraining method can effectively train the model to predict vehicle azimuth angles without knowing the concrete corresponding relationship between each azimuth angle and CSI.

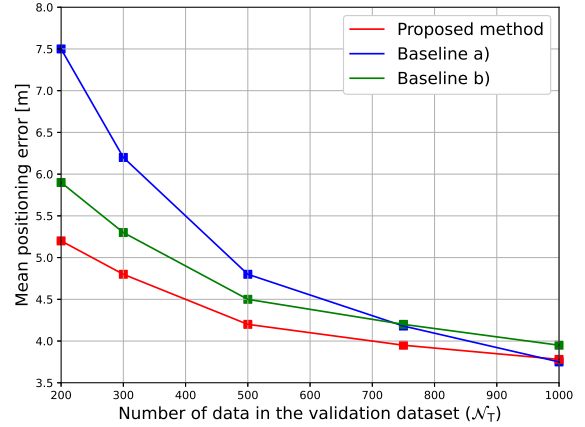
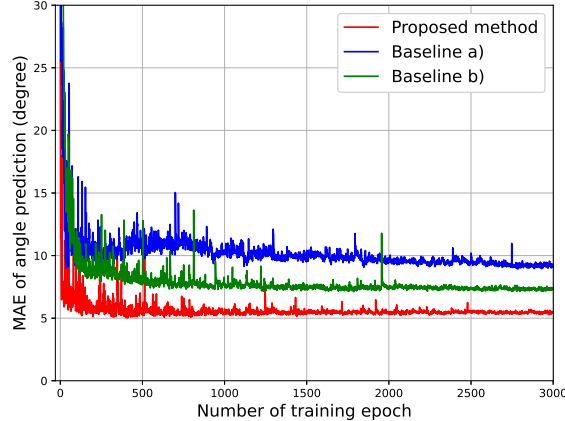
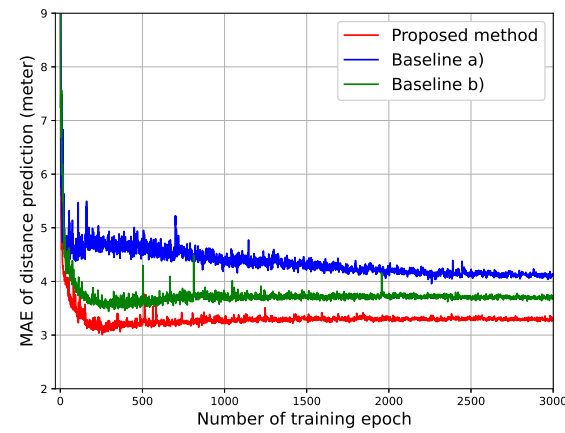
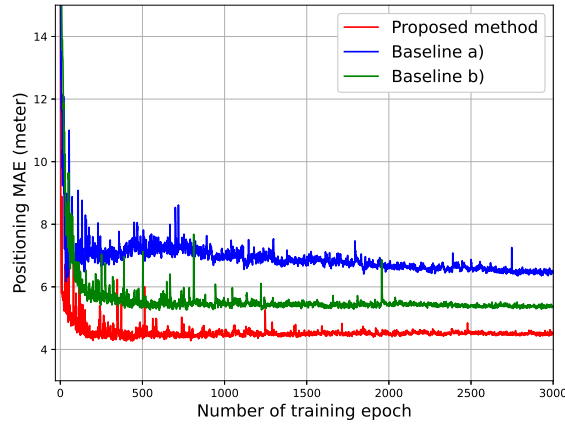


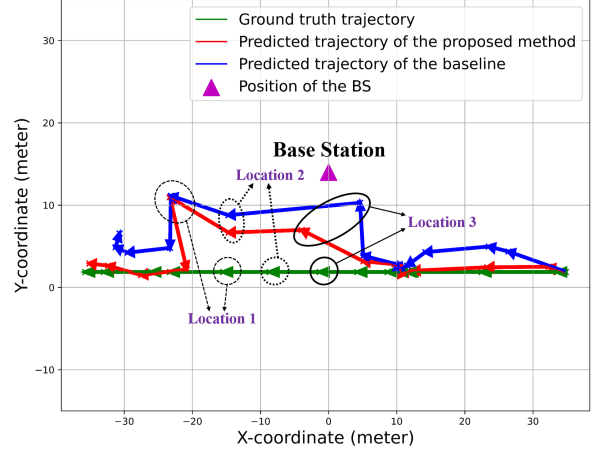
Fig. 14: Positioning error with different number of data in downstream training dataset.

2) *Downstream training:* In Fig. 14, we show how the mean positioning error changes as the number N_T of labeled data samples in the downstream training dataset varies. From this figure, we can see that the proposed algorithm can effectively improve the positioning accuracy especially when the amount of labeled training data samples is very small. Specifically, the proposed algorithm can reduce the mean positioning error by up to 30% when $N_T = 200$ compared to baseline a). This is because the proposed method pretrains the positioning model with a large amount of unlabeled data such that the pretrained model has a better generalization capacity. We can also observe that the proposed method can reduce the mean positioning error by up to 9.5% when $N_T = 200$ compared to baseline b). This stems from the fact that the pretraining labels of the proposed method contain the information of vehicle directions which is strongly correlated to the locations of vehicle. In contrast, the pretraining target of baseline b) is to minimize the contrastive loss between unlabeled CSI data, which is not related to vehicle positioning. As a result, the encoder of the proposed method can better extract features related to vehicle locations, and thus achieving lower positioning error.

In Fig. 15, we show how the MAEs of the azimuth angle and distance, and positioning errors change as the the number of training epochs increases. From Fig. 15 (a), we see that the proposed method reduces the MAE of azimuth angle from 9° to 5.5° compared to baseline a), and from 7.4° to 5.5° compared to baseline b). This stems from the fact that the proposed method pretrains the positioning model with images and a large number of unlabeled CSI data. Since the purpose of the pretraining of the proposed method is to predict the probability distribution vector of azimuth directions of each vehicle, which is strongly correlated to azimuth angle prediction, the trained model can achieve better accuracy on azimuth angle prediction compared to both baselines a) and b). From Fig. 15 (b), we observe that the proposed algorithm can respectively reduce the MAE of distance by up to 19% and 9% compared to baselines a) and b), which implies that the pretrained model also has better generalization capacity on vehicle-BS distance

(a) Validation MAE of predicted angle with $N_T = 300$.(b) Validation MAE of predicted distance with $N_T = 300$.(c) Training and validation positioning errors with $N_T = 300$.Fig. 15: Performance evaluation metrics with $N_T = 300$.

prediction despite that the pretraining labels do not explicitly include the distances between vehicles and the BS. This is because the prediction of the probability distribution vector of the vehicle azimuth direction needs to estimate the energy of multipath signals and distinguish the LoS and NLoS links [38]. Since the received signal strength depends on the distance between vehicle and the BS, the trained model may be able to extract features related to vehicle distance through pretraining,

Fig. 16: An example of vehicle positioning with $N_T = 300$.

and thus achieving better generalization capacity on vehicle-BS distance prediction. From Fig. 15 (c), we observe that, at the validation dataset, the proposed method can reduce the positioning error by up to 26% and 15% compared to baselines a) and b). These gains stem from the fact that the proposed method can effectively avoid overfitting since the proposed method can use pretraining to extract more useful features for positioning.

Fig. 16 shows an example of vehicle positioning. In this simulation, we randomly select 15 different points on the trajectory of a vehicle, and predict the coordinates of these locations using the proposed method and the baseline a) respectively. From this figure, we can see that the location coordinates estimated by the proposed method is closer to the ground truth trajectory compared to the baseline a), which implies that the proposed method can effectively improve the positioning accuracy when the amount of labeled training data is small. From Fig. 16, we can also see that there are three locations on the trajectory where the positioning accuracies are very low. This is because the communication links between vehicles and the BS are NLoS at these locations.

V. CONCLUSION

In this paper, we have designed a novel SSL framework that jointly uses a large sized unlabeled dataset that consists of images and unlabeled CSI data and a small sized labeled dataset that consists of CSI data and their corresponding position coordinates to estimate the positions of the vehicles served by the BS. The proposed framework consists of a pretraining stage and a downstream training stage. In the pretraining stage, the images are used to generate labels for unlabeled CSI data and thus pretraining the model. In the downstream training stage, the model will be retrained on the small sized labeled CSI dataset. Simulation results have shown that our proposed method can achieve higher positioning precision than the baseline with the same labeled dataset.

REFERENCES

- [1] J. A. del Peral-Rosado, J. A. López-Salcedo, S. Kim, and G. Seco-Granados, “Feasibility study of 5G-based localization for assisted driving,” in *Proc. International Conference on Localization and GNSS*, Barcelona, June 2016, pp. 1–6.
- [2] W. Shao, H. Luo, F. Zhao, Y. Ma, Z. Zhao, and A. Crivello, “Indoor positioning based on fingerprint-image and deep learning,” *IEEE Access*, vol. 6, pp. 74699–74712, November 2018.
- [3] C. Zhou, J. Liu, M. Sheng, Y. Zheng, and J. Li, “Exploiting fingerprint correlation for fingerprint-based indoor localization: A deep learning based approach,” *IEEE Transactions on Vehicular Technology*, vol. 70, no. 6, pp. 5762–5774, June 2021.
- [4] P. Wang, Toshiaki Koike A., and P. V. Orlik, “Fingerprinting-based indoor localization with commercial mmwave WiFi: NLOS propagation,” in *Proc. IEEE Global Communications Conference*, Taipei, Taiwan, December 2020, pp. 1–6.
- [5] X. Song, X. Fan, C. Xiang, Q. Ye, L. Liu, Z. Wang, X. He, N. Yang, and G. Fang, “A novel convolutional neural network based indoor localization framework with WiFi fingerprinting,” *IEEE Access*, vol. 7, pp. 110698–110709, August 2019.
- [6] C. Wu, X. Yi, W. Wang, L. You, Q. Huang, X. Gao, and Q. Liu, “Learning to localize: A 3D CNN approach to user positioning in massive MIMO-OFDM systems,” *IEEE Transactions on Wireless Communications*, vol. 20, no. 7, pp. 4556–4570, July 2021.
- [7] B. Zhang, H. Sifaou, and G. Y. Li, “CSI-fingerprinting indoor localization via attention-augmented residual convolutional neural network,” *IEEE Transactions on Wireless Communications*, vol. 22, no. 8, pp. 5583–5597, August 2023.
- [8] A. Foliadis, M. H. C. Garcia, R. A. Stirling-Gallacher, and R. S. Thomä, “CSI-based localization with CNNs exploiting phase information,” in *Proc. IEEE Wireless Communications and Networking Conference*, Nanjing, China, March 2021, pp. 1–6.
- [9] T. Wu, C. Pan, Y. Pan, H. Ren, M. Elkashlan, and C. Wang, “Fingerprint based mmWave positioning system aided by reconfigurable intelligent surface,” *IEEE Wireless Communications Letters*, vol. 12, no. 8, pp. 1379–1383, August 2023.
- [10] A. Foliadis, M. H. C. Garcia, R. A. Stirling-Gallacher, and R. S. Thomä, “Reliable deep learning based localization with CSI fingerprints and multiple base stations,” in *Proc. IEEE International Conference on Communications*, Seoul, Korea, May 2022, pp. 3214–3219.
- [11] K. He, X. Zhang, S. Ren, and J. Sun, “Deep residual learning for image recognition,” in *Proc. IEEE Conference on Computer Vision and Pattern Recognition*, Las Vegas, NV, USA, June 2016, pp. 770–778.
- [12] G. Charan and A. Alkhateeb, “Computer vision aided blockage prediction in real-world millimeter wave deployments,” in *Proc. IEEE Global Communications Conference Workshops*, Rio de Janeiro, Brazil, December 2022, pp. 1711–1716.
- [13] G. Charan, M. Alrabeiah, and A. Alkhateeb, “Vision-aided 6G wireless communications: Blockage prediction and proactive handoff,” *IEEE Transactions on Vehicular Technology*, vol. 70, no. 10, pp. 10193–10208, October 2021.
- [14] S. Jiang and A. Alkhateeb, “Computer vision aided beam tracking in a real-world millimeter wave deployment,” in *Proc. IEEE Global Communications Conference Workshops*, Rio de Janeiro, Brazil, December 2022, pp. 142–147.
- [15] M. Alrabeiah, A. Hredzak, and A. Alkhateeb, “Millimeter wave base stations with cameras: Vision-aided beam and blockage prediction,” in *Proc. IEEE Vehicular Technology Conference*, Antwerp, Belgium, May 2020, pp. 1–5.
- [16] B. Salehi, G. Reus-Muns, D. Roy, Z. Wang, T. Jian, J. Dy, S. Ioannidis, and K. Chowdhury, “Deep learning on multimodal sensor data at the wireless edge for vehicular network,” *IEEE Transactions on Vehicular Technology*, vol. 71, no. 7, pp. 7639–7655, July 2022.
- [17] J. Jiao, F. Li, Z. Deng, and W. Liu, “An indoor positioning method based on wireless signal and image,” in *Proc. International Congress on Image and Signal Processing, BioMedical Engineering and Informatics*, Datong, China, October 2016, pp. 656–660.
- [18] A. Alahi, A. Haque, and F. Li, “RGB-W: When vision meets wireless,” in *Proc. IEEE International Conference on Computer Vision*, Santiago, Chile, December 2015, pp. 3289–3297.
- [19] D. Dubois and H. Prade, “Probability theory in artificial intelligence : Judea Pearl . Probabilistic Reasoning in Intelligent Systems: Networks of Plausible Inference . San Mateo, CA: Morgan Kaufman, 1988. pp. xix + 552.,” *Journal of Mathematical Psychology*, vol. 34, no. 4, pp. 472–482, 1990.
- [20] S. Zhang, Z. Yang, M. Chen, D. Liu, K. Wong, and H. V. Poor, “Beam-forming design for the performance optimization of intelligent reflecting surface assisted multicast MIMO networks,” *IEEE Transactions on Wireless Communications*, to appear, July 2023.
- [21] W. Wang and W. Zhang, “Joint beam training and positioning for intelligent reflecting surfaces assisted millimeter wave communications,” *IEEE Transactions on Wireless Communications*, vol. 20, no. 10, pp. 6282–6297, October 2021.
- [22] Z. Zhu, C. Guo, R. Bao, M. Chen, W. Saad, and Y. Yang, “Positioning using visible light communications: A perspective arcs approach,” *IEEE Transactions on Wireless Communications*, to appear, March 2023.
- [23] Y. Yang, C. Li, R. Bao, C. Guo, C. Feng, and J. Cheng, “Multi-angle camera assisted received signal strength algorithm for visible light positioning,” *Journal of Lightwave Technology*, vol. 39, no. 23, pp. 7435–7446, December 2021.
- [24] D. Kang and D. Kum, “Camera and radar sensor fusion for robust vehicle localization via vehicle part localization,” *IEEE Access*, vol. 8, pp. 75223–75236, April 2020.
- [25] A. Bochkovskiy, C. Wang, and H. M. Liao, “YOLOv4: Optimal speed and accuracy of object detection,” *arXiv:2004.10934*, 2020.
- [26] D. Liu, P. Wang, T. Wang, and T. Abdelzaher, “Self-contrastive learning based semi-supervised radio modulation classification,” in *Proc. IEEE Military Communications Conference*, San Diego, CA, USA, November 2021, pp. 777–782.
- [27] M. Zhang and Z. Zhou, “M3MIML: A maximum margin method for multi-instance multi-label learning,” in *Proc. IEEE International Conference on Data Mining*, Pisa, Italy, December 2008, pp. 688–697.
- [28] S. Huang, W. Gao, and Z. Zhou, “Fast multi-instance multi-label learning,” *IEEE Transactions on Pattern Analysis and Machine Intelligence*, vol. 41, no. 11, pp. 2614–2627, November 2019.
- [29] X. Liu, F. Zhang, Z. Hou, L. Mian, Z. Wang, J. Zhang, and J. Tang, “Self-supervised learning: Generative or contrastive,” *IEEE Transactions on Knowledge and Data Engineering*, vol. 35, no. 1, pp. 857–876, January 2023.
- [30] P. H. Le-Khac, G. Healy, and A. F. Smeaton, “Contrastive representation learning: A framework and review,” *IEEE Access*, vol. 8, pp. 193907–193934, October 2020.
- [31] A. Foliadis, M. H. C. Garcia, R. A. Stirling-Gallacher, and R. S. Thomä, “Multi-environment based meta-learning with CSI fingerprints for radio based positioning,” in *Proc. IEEE Wireless Communications and Networking Conference (WCNC)*, Glasgow, United Kingdom, March 2023, pp. 1–6.
- [32] X. Tong, Z. Zhang, Y. Zhang, Z. Yang, C. Huang, K. Wong, and M. Debbah, “Environment sensing considering the occlusion effect: A multi-view approach,” *IEEE Transactions on Signal Processing*, vol. 70, pp. 3598–3615, June 2022.
- [33] K. He and J. Sun, “Convolutional neural networks at constrained time cost,” in *Proc. IEEE Conference on Computer Vision and Pattern Recognition*, Boston, MA, USA, June 2015, pp. 5353–5360.
- [34] M. Alrabeiah, J. Booth, A. Hredzak, and A. Alkhateeb, “ViWi vision-aided mmWave beam tracking: Dataset, task, and baseline solutions,” *arXiv:2002.02445*, 2020.
- [35] R. Kant, P. Saini, and J. Kumari, “Long short-term memory auto-encoder-based position prediction model for fixed-wing UAV during communication failure,” *IEEE Transactions on Artificial Intelligence*, vol. 4, no. 1, pp. 173–181, February 2023.
- [36] Z. Chen, Z. Zhang, Z. Xiao, Z. Yang, and R. Jin, “Deep learning-based multi-user positioning in wireless FDMA cellular networks,” *IEEE Journal on Selected Areas in Communications*, vol. 41, no. 12, pp. 3848–3862, December 2023.
- [37] S. Liu and W. Deng, “Very deep convolutional neural network based image classification using small training sample size,” in *Proc. Asian Conference on Pattern Recognition (ACPR)*, Kuala Lumpur, Malaysia, November 2015, pp. 730–734.
- [38] Z. Lin, T. Lv, and P. T. Mathiopoulos, “3-D indoor positioning for millimeter-wave massive MIMO systems,” *IEEE Transactions on Communications*, vol. 66, no. 6, pp. 2472–2486, June 2018.